Journal of Fluids and Structures 91 (2019) 102701

Contents lists available at ScienceDirect

Journal of Fluids and Structures

journal homepage: www.elsevier.com/locate/jfs

Flow-induced vibration of a cube orientated at different incidence angles

Jisheng Zhao *, John Sheridan, Kerry Hourigan, Mark C. Thompson

Fluids Laboratory for Aeronautical and Industrial Research (FLAIR), Department of Mechanical and Aerospace Engineering, Monash University, Melbourne, Victoria 3800, Australia

ARTICLE INFO

Article history:
Received 14 August 2018
Received in revised form 11 July 2019
Accepted 9 August 2019
Available online 22 August 2019

Keywords:
Flow-induced vibration
Bluff body wakes
Cube

ABSTRACT

This study experimentally investigates the transverse flow-induced vibration (FIV) of an elastically mounted cube at three different incidence angles of $\alpha = 0°$, $20°$ and $45°$, corresponding to two centreplane mirror-symmetric cases and one asymmetric case. The FIV response is characterised by analysing the vibration amplitude and frequency responses, together with the fluid force coefficients and phases, over the reduced velocity range of $1.2 \leqslant U^* \leqslant 16$. Here, $U^* = U/(f_{nw}H)$, with U the free-stream velocity, f_{nw} the natural frequency of the system in quiescent fluid (water) and H the frontal projected width of the body. It was found in the $\alpha = 0°$ case that two synchronisation regions could be identified, where the periodic body vibration was synchronised with oscillatory shear layers. The vibration amplitude was found to increase with U^* in the second synchronisation region, with the largest value of $A^*_{max} \simeq 0.74$ observed at the highest U^* value tested. In the asymmetric orientation case of $\alpha = 20°$, a synchronisation region occurred over $6.0 < U^* < 8.6$, where the amplitude tended to increase to its local peak of $A^*_{max} \simeq 0.25$ at $U^* = 8.6$. For higher U^* values, synchronisation was lost, but the cube still exhibited high amplitude oscillations. However, in the $\alpha = 45°$ case, while the vibration amplitude tended to increase with U^* (i.e. $A^*_{max} \approx 0.3$ at $U^* = 16$), the FIV response was found to be desynchronised over the entire U^* range. The findings indicate that body vibration is strongly coupled with the oscillatory separating shear layers for all α cases, which can result in significant vibration.

1. Introduction

This study reports on an experimental investigation of the transverse flow-induced vibration (FIV) of an elastically mounted cube, where the flow is perpendicular to the vertical axis of the body, and the cube is constrained to move in the cross-flow direction only. As such, this research falls under the broader framework of investigations of FIV of bluff bodies. The prevalence and importance of FIV of structures in a variety of engineering applications, from being an undesirable phenomenon on structures (e.g. offshore oil platforms, high-rise buildings) to a potential energy-harvesting source (see Wang et al., 2017; Soti et al., 2018), has motivated numerous research works in the past half a century that aim to characterise, predict and suppress/enhance FIV. Comprehensive reviews on the subject of FIV have been provided by Blevins (1990), Sarpkaya (2004), Williamson and Govardhan (2004), Naudascher and Rockwell (2005) and Païdoussis et al. (2010). Most of previous FIV studies have focused on two-dimensional cylindrical bodies. On the other hand,

* Corresponding author.
E-mail address: jisheng.zhao@monash.edu (J. Zhao).

https://doi.org/10.1016/j.jfluidstructs.2019.102701
0889-9746/

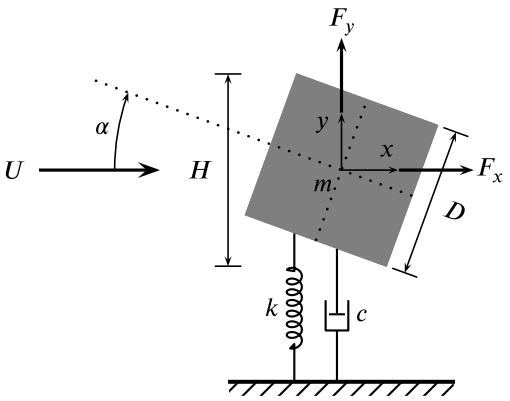

Fig. 1. Definition sketch for the transverse-only FIV of a cube. The hydro-elastic system is simplified as a 1-DOF system constrained to move in the cross-flow direction: the oncoming free-stream velocity is denoted by U; the frontal projected width of the cube is denoted by H; the angle of attack is denoted by α; the oscillating mass is denoted by m, the structural damping is denoted by c, and the structural stiffness is denoted by k; F_x and F_y represent the drag and the transverse lift forces, respectively.

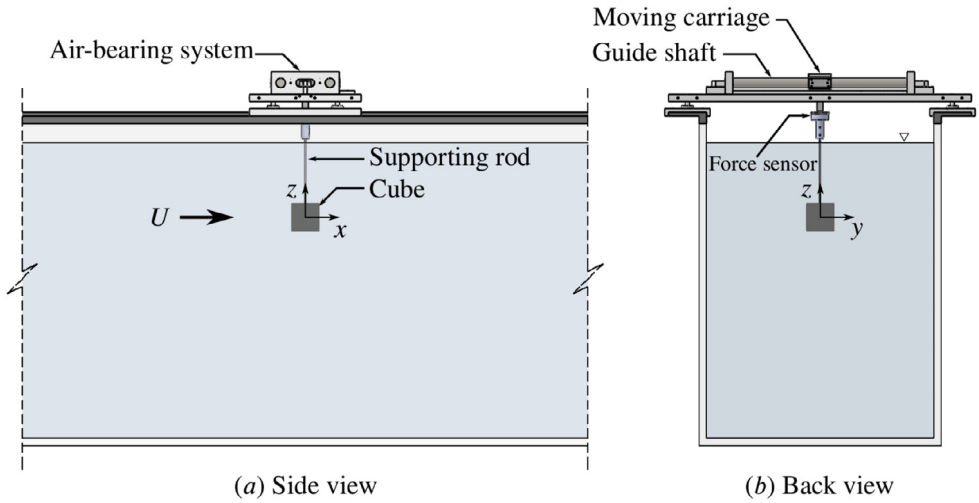

Fig. 2. Schematic of the experimental set-up from the side and back views. The cube is vertically (in z direction) supported by a rod that is mounted to a force sensor coupled with the air-bearing system, with a single degree of freedom to vibrate transversely (in y direction) to a free-stream flow (in x direction).

Table 1
The natural frequencies of the system at the three α values tested.

α	H [mm]	f_{na} [Hz]	f_{nw} [Hz]	ζ
0°	70.0	0.557	0.520	1.39×10^{-3}
20°	89.9	0.275	0.256	2.57×10^{-3}
45°	99.0	0.395	0.369	2.00×10^{-3}

however, FIV of cubic structures has received much less attention, despite its importance in many engineering applications, such as construction loads lifted on (tower) cranes, sling loads carried by helicopters, cable cars, vehicles, fish cages and offshore platforms, where the structures may experience undesirable FIV phenomena in winds or ocean currents that can affect the structural performance and even safety. Thus, apart from motivations arising from its practical importance of the problem, the principal aim of the present investigation is to gain a fundamental understanding of the FIV mechanism of a cube as a generic three-dimensional bluff body with sharp edges.

Since the pioneering experiments of Brooks (1960), FIV of cylindrical bluff bodies, including circular, D-section, square and rectangular cross-sectioned cylinders, have been extensively studied (e.g. Feng, 1968; Bearman et al., 1987; Nakamura et al., 1991; Khalak and Williamson, 1996, 1997; Govardhan and Williamson, 2000; Nemes et al., 2012; Massai et al., 2018; Zhao et al., 2014a,b, 2018a). In particular, two different body oscillator phenomena typical of FIV, namely *vortex-induced vibration (VIV)* and *galloping*, have been the focus of much of the prevalent research. VIV occurs as vortices are shed

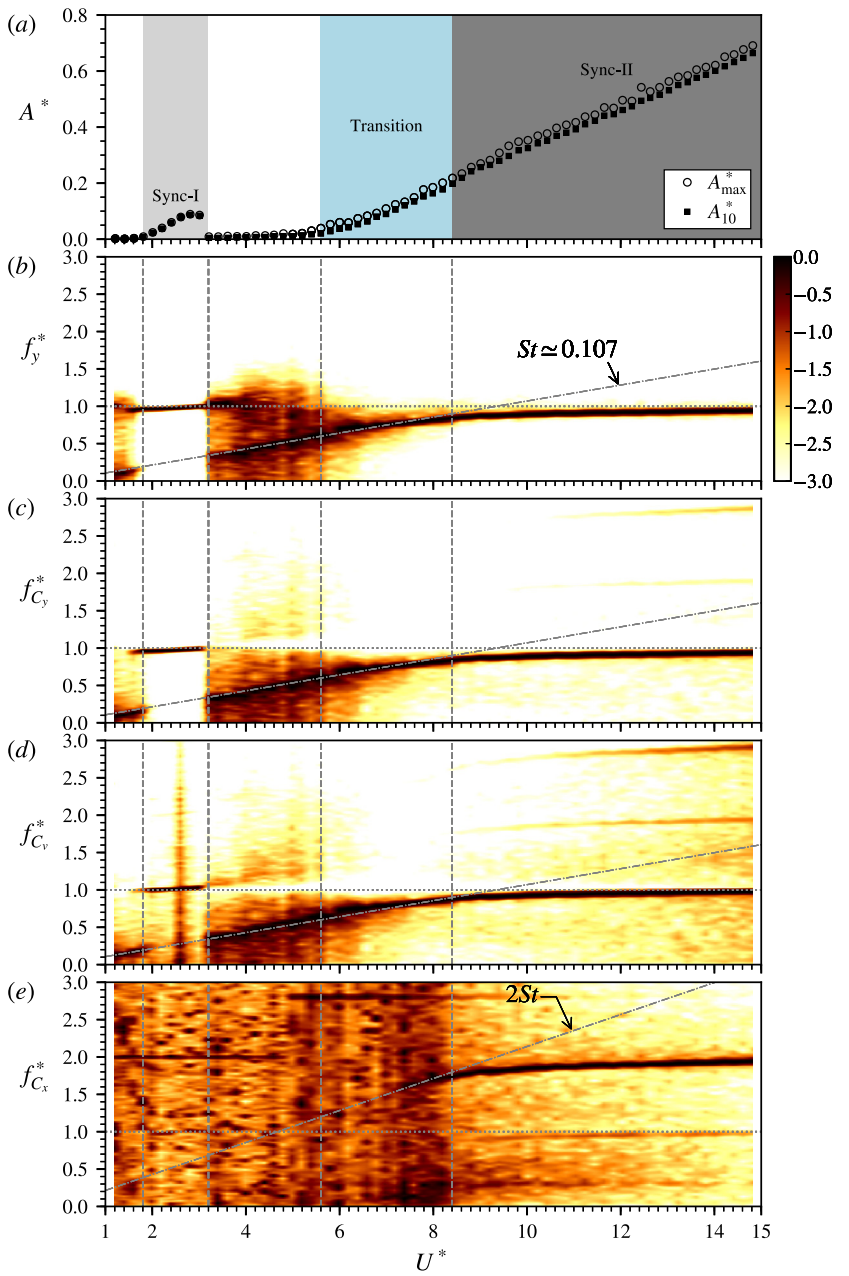

Fig. 3. The amplitude response and the logarithmic-scale normalised frequency power spectral density contours as a function of the reduced velocity for the case of $\alpha = 0°$. The vertical dashed lines represent boundaries between different FIV regions. Here the non-dimensionalised frequencies correspond to: f^*_y, the (normalised) transverse cube frequency; and $f^*_{C_y}, f^*_{C_v}, f^*_{C_x}$ are the frequencies corresponding to the total transverse force, the vortex force and the streamwise force, respectively. All frequencies are normalised by the natural frequency of the system, f_{nw}.

alternatively from sides of an elastic or elastically mounted body. These vortices, in turn, create a fluctuating pressure distribution that can result in a significant vibration response over certain flow velocity ranges when the vortex shedding frequency and the body vibration frequency are synchronised. To fundamentally characterise VIV, circular cylinders have been adopted as a standard model, due to their geometric simplicity and *axial symmetry* that prohibits the occurrence of another FIV form, namely galloping. On the other hand, structures with an *axial asymmetry* (e.g. D-section and square cylinders) may be susceptible to galloping, as opposed to, or in combination with, VIV. Unlike VIV, which is excited by the vortex shedding instability and thus exhibits limited vibration amplitude (generally of the order of one body diameter), galloping is driven by unsteady aerodynamic forces that arise from the body movement and thus can result in large body

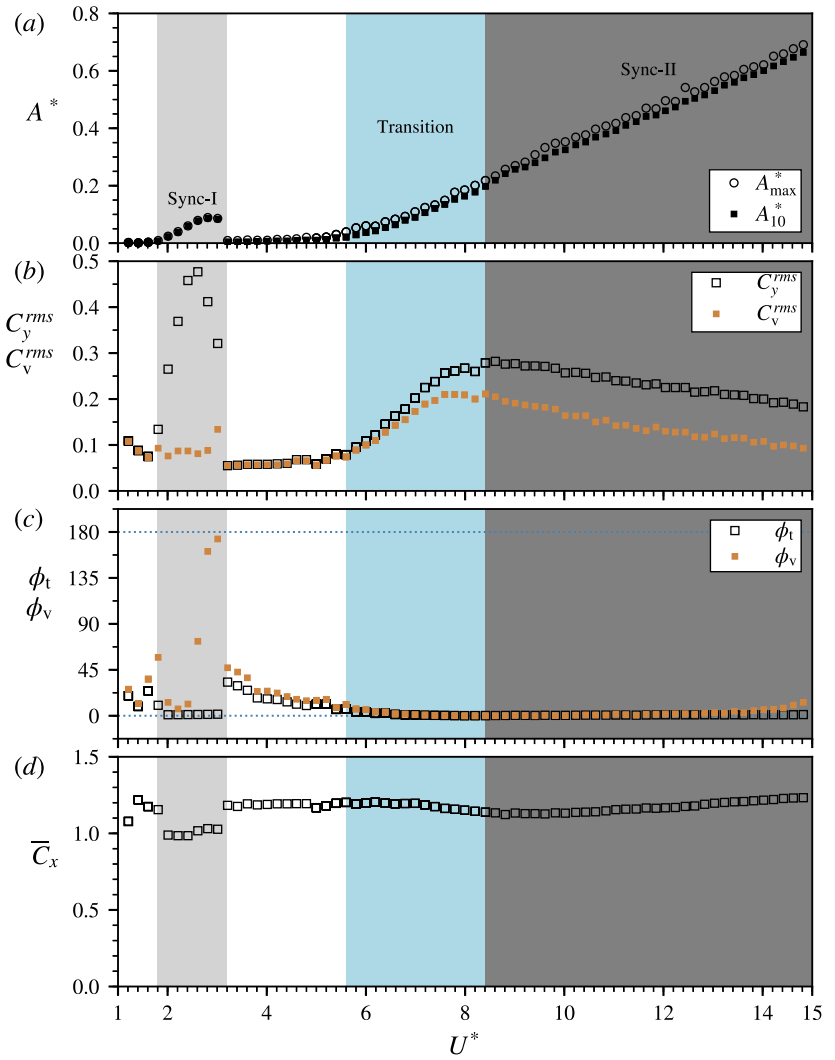

Fig. 4. Fluid forces and phases (in degrees) as a function of the reduced velocity for the $\alpha = 0°$ case. Note that (*a*) revisits the amplitude response; the two synchronisation regions are shaded grey, while the transition region is shaded light blue. The variables plotted as follows: the total and vortex rms transverse force coefficients, C_y^{rms} and C_v^{rms}; the total and vortex phase of these coefficients, ϕ_t and ϕ_v (in degrees); and the mean downstream force coefficient, $\overline{C}_x$. (For interpretation of the references to colour in this figure legend, the reader is referred to the web version of this article.)

oscillations with the amplitude increasing with the flow velocity, and a frequency much lower than that of the vortex shedding (Zhao et al., 2018a).

Recently, Nemes et al. (2012) found that for a square cylinder with low mass-damping ratio in water-channel experiments, the FIV response exhibited three regimes in a parameter space of the flow incidence angle (α) and the reduced velocity (U^*), namely a galloping regime at low angles of attack of $0° \leqslant \alpha < 7.5°$, a combined VIV-galloping regime at medium angles of attack of $10° < \alpha \leqslant 22.5°$ and a VIV regime at high angles of attack of $25° \leqslant \alpha \leqslant 45°$. Note that the reduced velocity here is defined by $U^* = U/(f_{nw}H)$, where U is the free-stream velocity, H is the frontal projected width of the body, and f_{nw} is the natural frequency of the system in quiescent fluid (water). Subsequently, Zhao et al. (2014b, 2018c) provided further detailed analyses on the fluid–structure synchronisation and wake modes at three representative α values of 0°, 20° and 45° for the three FIV response regimes.

Much less attention has been paid to the FIV of three-dimensional geometries. The transverse FIV of a sphere, a generic symmetrical three-dimensional prototype, was reported for the first time by Govardhan and Williamson (2005), showing a VIV response over a wide U^* range. On the other hand, even less research has been conducted on the problem of flow past a cube, despite its practical importance in many engineering applications. Klotz et al. (2014) experimentally studied the wake behind a fixed cube with a face normal to the flow over $100 \leqslant Re \leqslant 400$, and observed two flow bifurcations. This followed on from the numerical study of Saha (2004) and Saha (2006) who tracked the wake flow

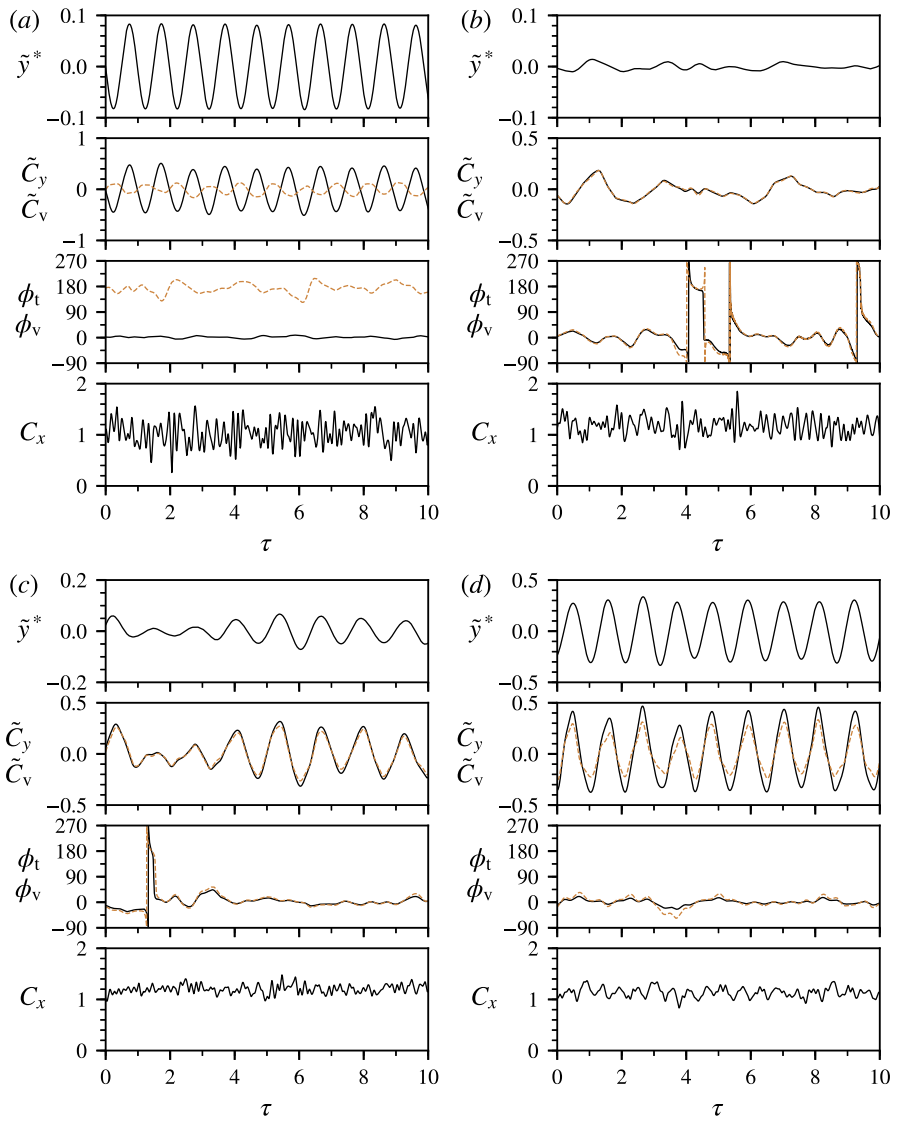

Fig. 5. Sample time traces for the $\alpha = 0°$ case at four selected reduced velocities: $U^* = 3.0$ in (*a*), $U^* = 5.0$ in (*b*), $U^* = 7.0$ in (*c*) and $U^* = 10.0$ in (*d*). It should be noted that $\tilde{y}^*$ represents the fluctuation component of the normalised body displacement, namely $\tilde{y}^* = y^* - \overline{y}^*$ with $y^* = y/H$ and $\overline{y}^* = \overline{y}/H$ (the time-averaged component); similarly, $\tilde{C}_y = C_y - \overline{C}_y$ and $\tilde{C}_v = C_v - \overline{C}_v$.

transitions over a similar Reynolds number range. Interestingly, the post-transition wake states and transition Reynolds numbers are a reasonable match for those of a sphere. The two-tailed and hairpin looped wake observed for a sphere also occurs for the cube. However, Saha (2004) also showed that the force coefficients display some difference for those of a sphere. In addition, in the near wake, there are weaker counter-rotating vortex pairs emanating from each of the four downstream corners. Given these distinct similarities and differences between the two cases, it seems intriguing to investigate the fluid–structure interaction of an elastically mounted cube with sharp edges, which, to the authors' knowledge, has remained largely unknown.

The present study aims to examine the transverse FIV response of a cube at the aforementioned three angles of attack, $\alpha = 0°$, 20° and 45°, as a function of U^*. The selection of these representative angles of attack will allow a direct comparison of the FIV responses of a cubic and its counterpart two-dimensional square cylinder. More specifically, it experimentally characterises the structural response, fluid forces and near-field flow structures. The article proceeds by describing the fluid–structure system modelling and the experimental details in Section 2. The results and discussion on the structural vibration response are presented in Section 3. Finally, conclusions are drawn in Section 4.

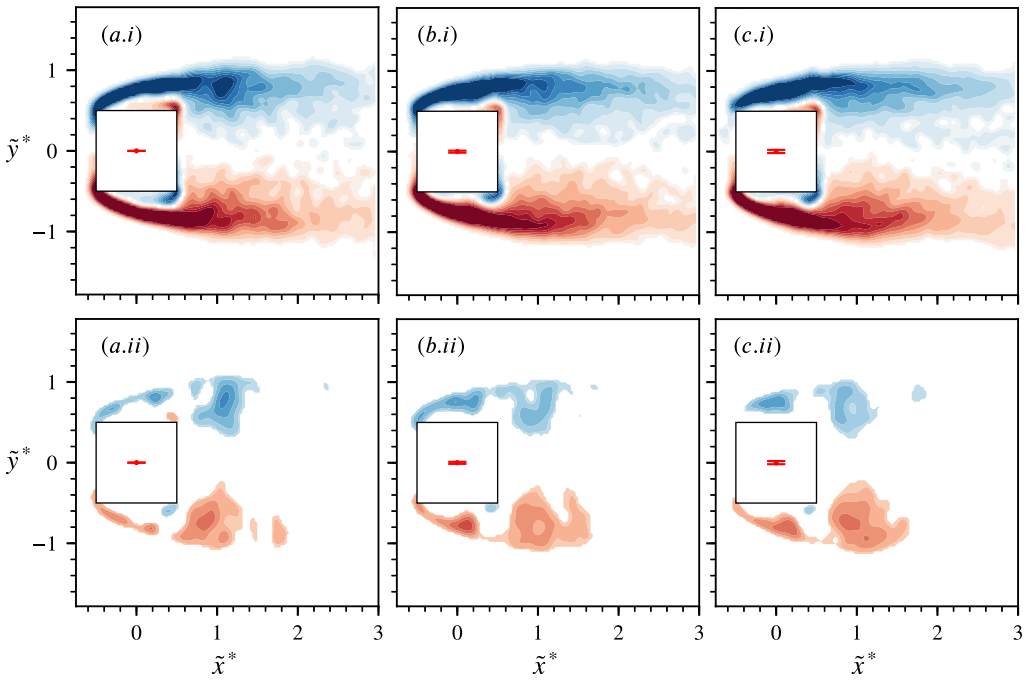

Fig. 6. Phase-averaged vorticity (top row) and swirling strength (bottom row) contours showing flow separations from the forward corners at (*a*) $U^* = 1.4$, (*b*) $U^* = 4.0$ and (*c*) $U^* = 5.0$ for $\alpha = 0°$. The normalised vorticity range shown here is $\omega^* \in [-4, 4]$ (with 21 levels); the normalised swirling strength range is $\pm\lambda_{ci}^2 \in [-0.35, 0.35]$ (with 21 levels). In each plot, the vertical line between two horizontal bars in red represents the peak-to-peak vibration amplitude. See supplementary movies 1–3 for the full oscillation cycles. (For interpretation of the references to colour in this figure legend, the reader is referred to the web version of this article.)

2. Experimental details

The fluid–structure system in the present study is modelled based on a linear mass–spring–damper (MSD) system with one degree of freedom (1-DOF) to move transversely to an oncoming fluid flow, as schematically shown in Fig. 1. Thus, the governing equation of motion is described by

$$m\ddot{y} + c\dot{y} + ky = F_y\,, \tag{1}$$

where m is the total oscillating mass of the system, c is the structural damping factor, k is the spring constant, y is the body displacement, and F_y is the lift force of the fluid on the cube. Here, the dots placed over the variables indicate time derivatives.

A schematic of the experimental setup is shown in Fig. 2. The MSD system was experimentally modelled by employing a low-friction air-bearing system which provided low structural damping and precisely constrained the body motion to be in the direction transverse to the oncoming free-stream. The structural stiffness was controlled by extension springs attached to both sides of a slider carriage. More details and validation studies of the air-bearing system can be found in Wong et al. (2017, 2018) and Zhao et al. (2018a,b). The cube model was vertically supported by a thin rod that was adapted to a force sensor coupled with the carriage. The present experiments were conducted in the recirculating free-surface water channel of the *Fluids Laboratory for Aeronautical and Industrial Research (FLAIR)* at Monash University, Australia. The test section of the water channel has dimensions of 600 mm in width, 800 mm in depth and 4000 mm in length. The free-stream velocity in the present experiments could be varied continuously over the range $50 \leqslant U \leqslant 450$ mm s^{-1} (see Zhao et al., 2014a,b), while the free-stream turbulence level was found to be less than 1%.

The cube model used, which was precision machined from Acetal plastic, had a side width of $D = 70$ mm $\pm$ 0.010 mm. The cylindrical support rod, made from tungsten carbide for extra stiffness and to maintain straightness, had a diameter of 3 mm, giving a ratio between the cube width and the support rod diameter of 23.3. The total immersed length of the rod was $L \simeq 175$ mm ($2.5D$), which was set to minimise free-surface effects, according to the experiments by Mirauda et al. (2014) and verified by Sareen et al. (2018b), which showed free-surface effects were negligible for flow past a sphere when it was placed at least one diameter below the free surface. The total oscillating mass was $m = 1746.4$ g, and the displaced mass of the fluid was $m_\mathrm{d} = \rho\pi D^3 = 342.9$ g (with ρ the fluid density), giving a mass ratio of $m^* = m/m_\mathrm{d} = 5.09$. The natural frequencies in both air (f_{na}) and water (f_nw) and structural damping ratio (ζ) of the system were measured by conducting free decay tests individually in air and in quiescent water. Table 1 shows the values of these parameters for the three α values tested. Here, the structural damping ratio was determined with consideration of the added mass by

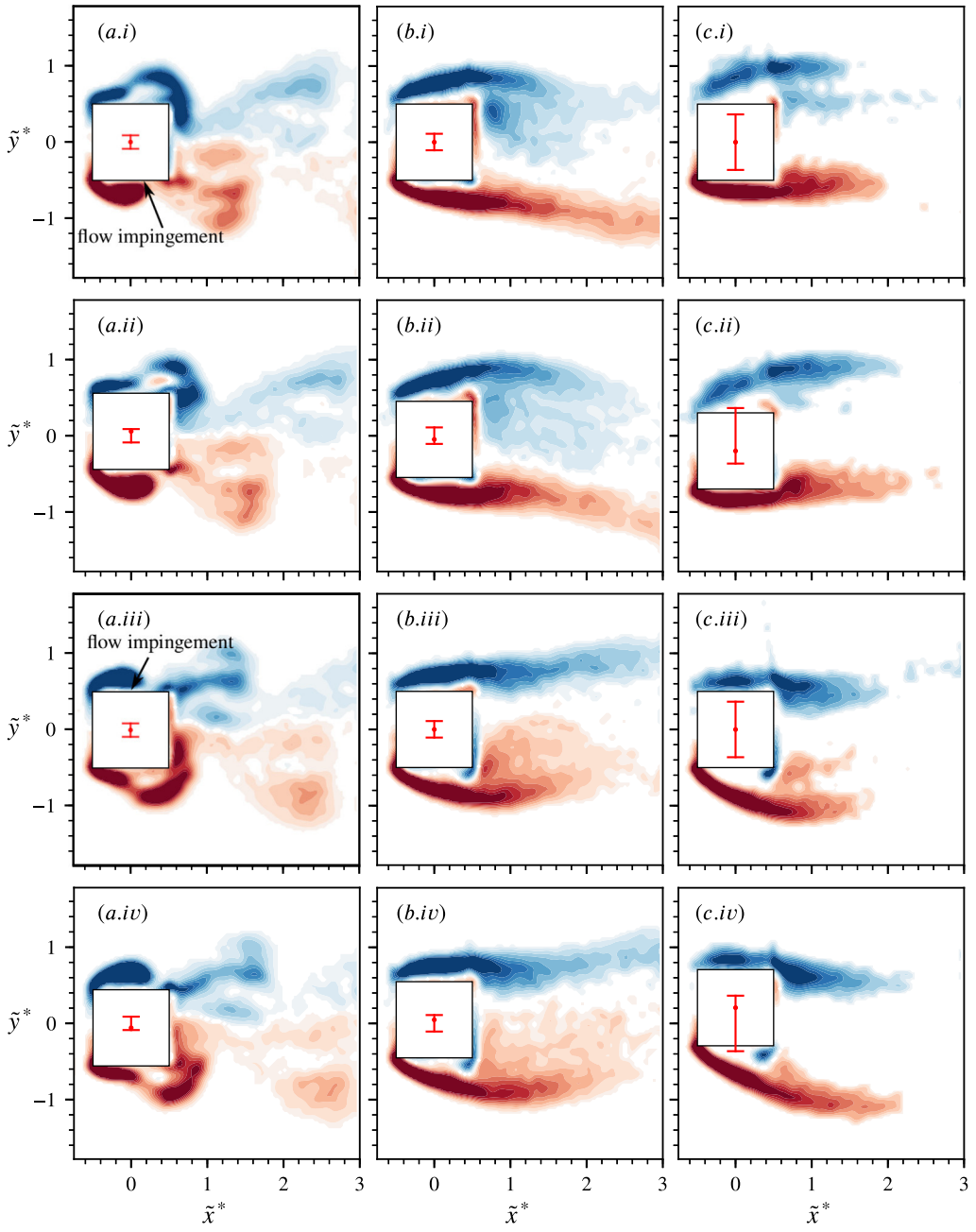

Fig. 7. Phase-averaged vorticity contours at (*a*) $U^* = 3.0$ from the Sync-I region, (*b*) $U^* = 7.0$ from the transition region and (*c*) $U^* = 10.0$ from the Sync-II region of the $\alpha = 0^\circ$ case. See supplementary movies 4–6 for the full oscillation cycles. For more details, refer to the caption for Fig. 6.

$\zeta = c/(2\sqrt{k(m + m_A)})$, where $m_A = ((f_{na}/f_{nw})^2 - 1)m$ is the added mass. It should be noted that the spring stiffness was varied in order to achieve similar U^* ranges for the α cases with different H values, which resulted in different values of f_{na}, f_{nw} and ζ for the α cases.

The body displacement was measured using a non-contact digital optical linear encoder (model: RGH24; Renishaw, UK) with a measurement range of ±200 mm and a resolution of 1 μm. While the drag force (F_x) was measured directly by the force sensor (model: Mini40; ATI-IA, USA), the transverse lift force (F_y) acting on the vibrating body was determined based on Eq. (1). This force sensor had an accuracy of 5 mN in both F_x and F_y. Details of the force measurement technique have been given by Zhao et al. (2014b, 2018b). The measurements were sampled at 100 Hz for 300 s. More details of the data acquisition system can be found in Wong et al. (2017) and Zhao et al. (2018b). In the present study, the FIV response was investigated over the reduced velocity range of $1.2 \leqslant U^* \leqslant 16$. The corresponding Reynolds number range

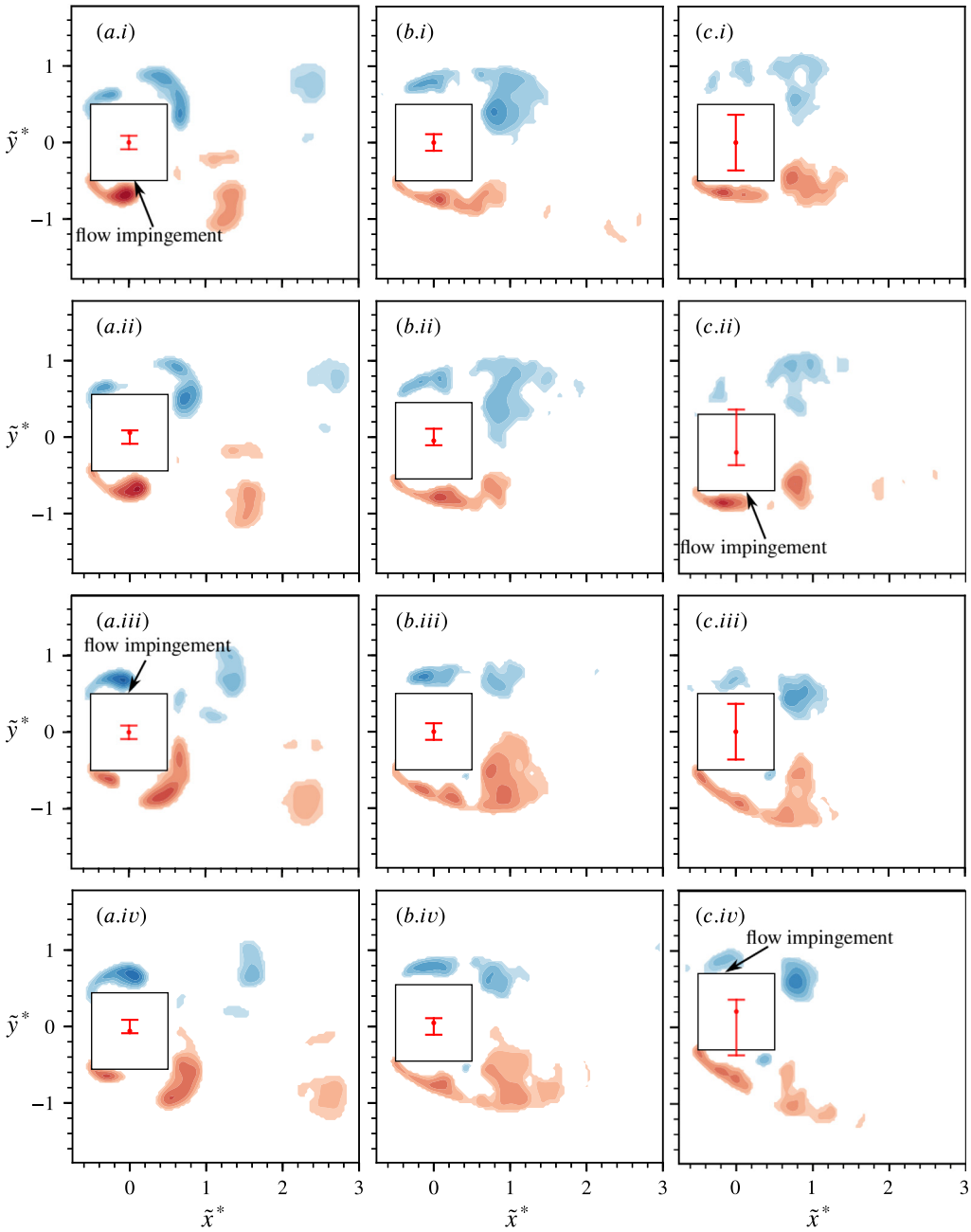

Fig. 8. Swirling strength contours at (*a*) $U^* = 3.0$ from the Sync-I region, (*b*) $U^* = 7.0$ from the transition region and (*c*) $U^* = 10.0$ from the Sync-II region of the $\alpha = 0°$ case. For more details, refer to the caption for Fig. 6.

was $2840 \leqslant Re \leqslant 36\,595$. Here, the Reynolds number based on the frontal projected width of the body is defined by $Re = UH/\nu$, with ν the kinematic viscosity of the fluid.

The near-wake flow structures were examined using the particle image velocimetry (PIV) technique. Since details of the PIV system used have been provided by Zhao et al. (2018a,b), only a brief summary is presented here. The flow was seeded with hollow micro-spheres (model: Sphericel 110P8; Potters Industries Inc.) having a nominal diameter of 13 μm and a specific weight of 1100 kg m^{-3}. The horizontal illumination laser sheet (3 mm in thickness) was produced using a continuous laser (model: MLL-N-532-5 W; CNI, China). The PIV imaging was performed using a high-speed camera (model: Dimax S4; PCO AG, Germany) with a resolution of 2016 pixel × 2016 pixel. This camera was equipped with a 50 mm lens (Nikon Corporation, Japan), giving a magnification factor of 7.51 pixels/mm for the field of view of interest. For each PIV imaging case, a set of 3100 image pairs was captured at a sampling rate of 10 Hz for quantitative analysis. To

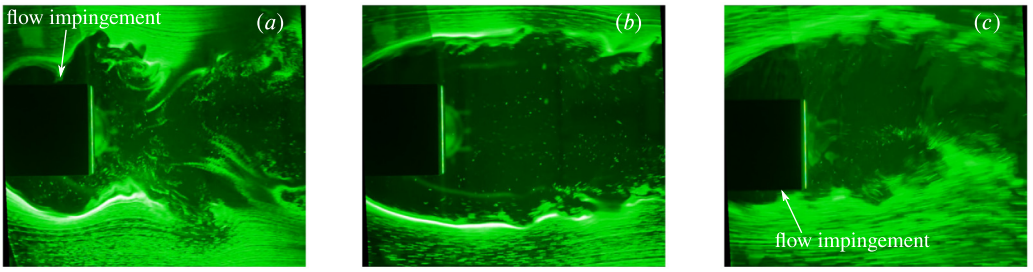

Fig. 9. Hydrogen-bubble flow visualisations demonstrating flow impingement in the two synchronisation regions, compared with the negligible vibration region: (*a*) $U^* = 3.0$ (Sync-I), (*b*) $U^* = 4.0$ (non-vibration region) and (*c*) $U^* = 10.0$ (Sync-II) for $\alpha = 0°$. See supplementary movies 7–9.

better understand the evolution of the wake structures, images of each set were sorted into 24 phases based on the body's displacement and velocity, yielding at least 120 image pairs for averaging. The PIV data was processed using validated in-house PIV software developed by Fouras et al. (2008), with 32×32 pixel^2 interrogation windows in a grid layout with 50% window overlap.

3. Results and discussion

3.1. Vibration response at $\alpha = 0°$

Fig. 3 presents the normalised body vibration amplitude (A^*) as a function of the reduced velocity for the $\alpha = 0°$ case, together with the normalised frequency responses of the body displacement, the transverse lift, the vortex force and the drag force, namely f_y^*, $f_{C_y}^*$, $f_{C_v}^*$ and $f_{C_x}^*$. Note that the normalised amplitude is defined by $A^* = A/H$, with $A_{\max}^*$ denoting the local maximum value and A_{10}^* denoting the mean of the top 10% values at a given U^*. The frequency components in Fig. 3 (*b*)–(*e*) are normalised by the natural frequency f_{nw} (i.e. $f^* = f/f_{\mathrm{nw}}$), while the power spectral density (PSD) contours are normalised by their local peak value and presented in logarithmic scale. In this study, the drag coefficient is defined by $C_x = F_x/(\frac{1}{2}\rho U^2 HL)$, while the transverse lift and the vortex force coefficients are defined by $C_y = F_y/(\frac{1}{2}\rho U^2 HL)$ and $C_{\mathrm{v}} = F_{\mathrm{v}}/(\frac{1}{2}\rho U^2 HL)$, respectively, where $F_{\mathrm{v}} = F_y - F_{\mathrm{p}}$, with $F_{\mathrm{p}} = -m_{\mathrm{A}}\ddot{y}$ the potential force (see Lighthill, 1986; Govardhan and Williamson, 2000; Morse and Williamson, 2009; Zhao et al., 2014b).

As can be seen from Fig. 3(*a*), there are three vibration regions observed with significant body oscillations, namely two synchronisation regions (Sync-I and Sync-II shaded grey) where the body vibration frequency is synchronised with the transverse lift frequency, and one transition region (shaded light blue) where the fluid–structure system develops gradually from a negligible vibration state to a synchronisation state (Sync-II) as U^* is increased.

The first synchronisation region (Sync-I) occurs over the reduced velocity range of $1.8 < U^* \leqslant 3.0$, which is bounded by two non-vibration regions on both sides. Upon the occurrence of synchronisation, the body vibration becomes highly periodic with the body vibration frequency locking onto the natural frequency of the system in quiescent water ($f_y^* \simeq 1$ in Fig. 3(*b*)). As U^* is increased, the vibration amplitude tends to increase to reach a local peak of $A^* \simeq 0.09$ at $U^* = 2.8$, prior to a sharp drop to $A^* \simeq 0$ at $U^* = 3.2$. On the other hand, as shown in Fig. 5(*b*), the root-mean-square coefficient (rms) of the transverse lift (C_y^{rms}) exhibits a "bell shape" over this region, increasing rapidly to reach its peak of $C_y^{rms} \simeq 0.48$ at $U^* = 2.6$ and afterwards decreasing sharply to its minimum ($C_y^{rms} \simeq 0.06$) at $U^* = 3.2$; however, no significant changes are observed in the root-mean-square coefficient of the vortex force ($C_{\mathrm{v}}^{rms} \approx 0.09$), which is different from other cases of cylindrical bluff bodies exhibiting significant variations in C_{v}^{rms} in their VIV lock-in regions (e.g. circular cylinders in Zhao et al. (2014a), square cylinders in Zhao et al. (2014b), D-section cylinders in Zhao et al. (2018a)). Furthermore, as shown in Fig. 4(*c*), the total phase (the phase angle between the transverse lift and the body displacement, denoted by ϕ_{t}) remains consistent at 0° in the Sync-I region, while the vortex phase (the phase angle between the vortex force and the body displacement, denoted by ϕ_{v}) undergoes a sharp jump from 0° to 180° at $U^* \approx 2.6$, around which the vortex force frequency response in Fig. 3(*d*) sees a narrow region exhibiting broadband components. It should also be noted that the drag frequency response (Fig. 3(*e*)) in general exhibits broadband noise over the Sync-I region, indicating that the drag force is highly aperiodic in this region. To demonstrate the vibration dynamics in the Sync-I region, Fig. 5(*a*) presents sample time traces at $U^* = 3.0$ as a representative reduced velocity. The above results suggest that the vibration mechanism in the Sync-I region is likely to be different from that often seen with cylindrical bluff bodies. In fact, this vibration region is found to be associated with flow impinging behaviour on both sides of the body, rather than the near-wake vortex shedding. Further discussion will be given by examining the near-body flow structure through PIV measurements.

The transition region occurs over the reduced velocity range of $5.6 < U^* < 8.4$. In this region, while the oscillation amplitude tends to increase with U^* ($A_{\max}^* \simeq 0.22$ at $U^* = 8.4$), the frequency response still exhibit broadband frequency components. However, the dominant component of f_y^*, $f_{C_y}^*$ and $f_{C_{\mathrm{v}}}^*$ deviates from the trend of the Strouhal vortex shedding

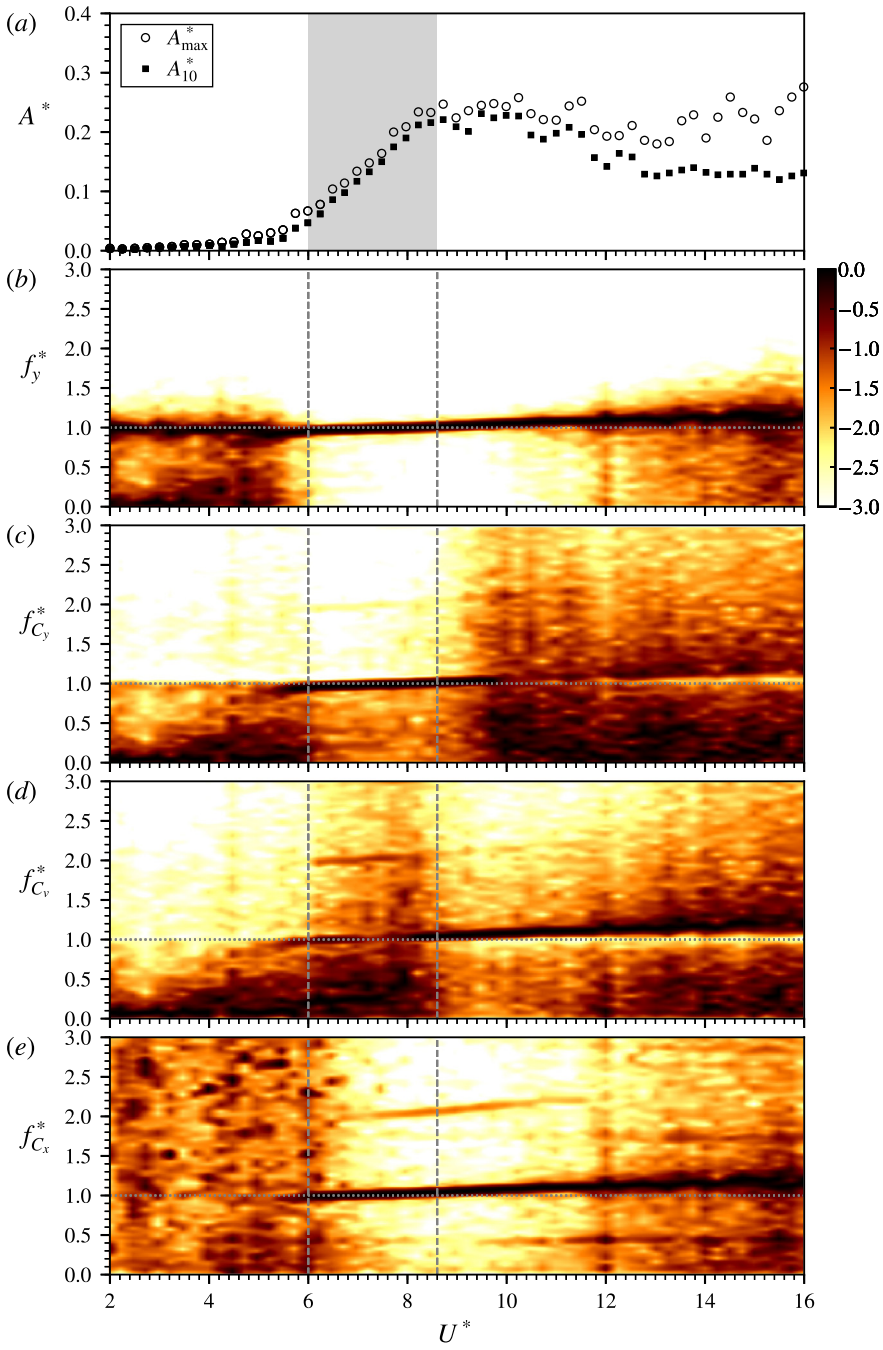

Fig. 10. The amplitude response and the logarithmic-scale normalised frequency power spectral density contours as a function of the reduced velocity for the case of $\alpha = 20°$. The synchronisation region is shaded grey, while the vertical dashed lines represent boundaries of the synchronisation region.

frequency ($St \simeq 0.107$) and increases gradually towards f_{nw}, and the dynamics also gradually becomes periodic (see sample traces at $U^* = 5.0$ and 7.0 for comparison in Fig. 5(*b*) and (*c*)). On the other hand, both C_y^{rms} and C_v^{rms} tend to increase to reach their local peaks ($C_y^{rms} \simeq 0.28$ and $C_v^{rms} \simeq 0.21$) at $U^* = 8.4$, while both ϕ_t and ϕ_v remain consistently close to 0°. Despite a notable increase in the vibration amplitude, $\overline{C}_x$ is found to decrease very slightly from 1.20 to 1.14 over this region.

Further increasing U^* sees the second synchronisation region, Sync-II, where the body vibration amplitude continues to increase to reach $A^*_{max} \simeq 0.74$ at the highest U^* tested, while the vibration frequency appears to gradually lock onto f_{nw}.

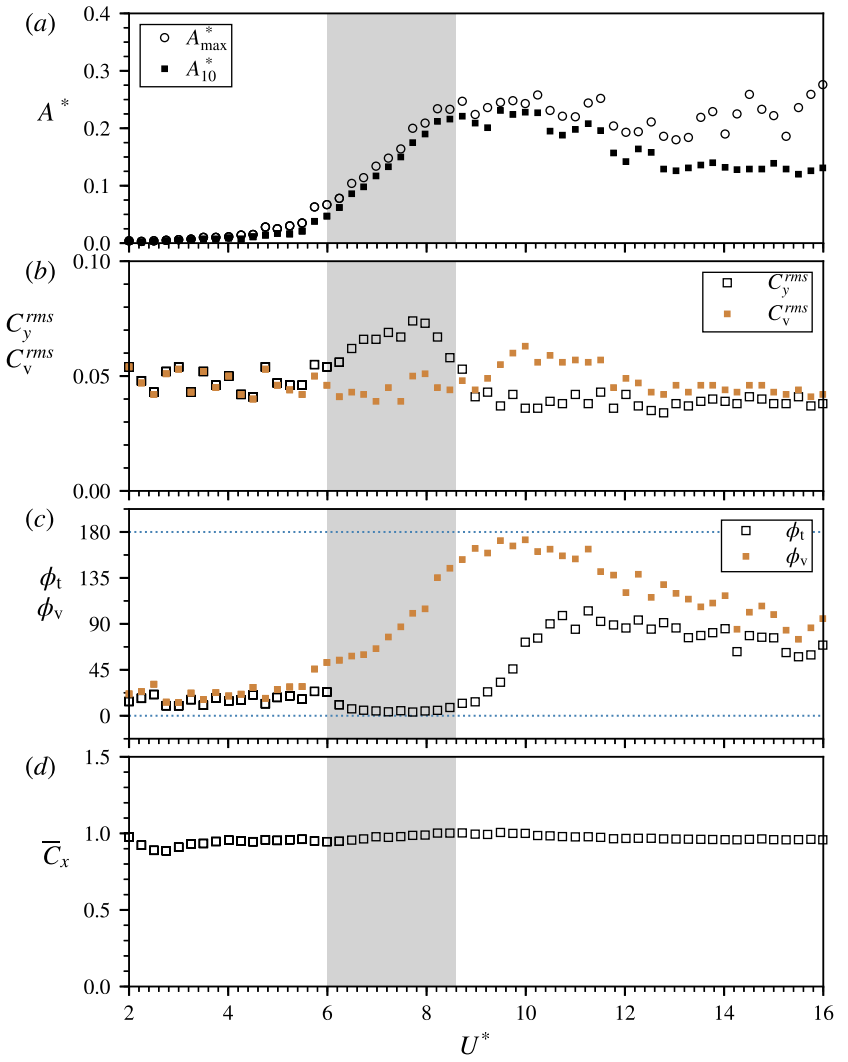

Fig. 11. Fluid forces and phases as a function of the reduced velocity for the $\alpha = 20°$ case. Note that (*a*) revisits the amplitude response; the synchronisation region is shaded grey.

Similar to the Sync-I region, the body vibration in this region is highly periodic. It is interesting to note that the frequency responses of $f^*_{C_y}$ and $f^*_{C_v}$ exhibit weak harmonics at $2f_{nw}$ and $3f_{nw}$ which tend to become stronger as U^* is increased. Unlike the Sync-I region and the transition region, the $f^*_{C_x}$ response shows its dominant component at $2f_{nw}$, indicating that the drag force becomes relatively periodic in this region. To demonstrate the vibration dynamics, Fig. 5(*d*) shows sample time traces at $U^* = 10.0$. Moreover, both C_y^{rms} and C_v^{rms} tend to decrease gradually, while $\overline{C}_x$ remains fairly stable at 1.14. It should also be noted that both ϕ_t and ϕ_v remain close to 0°. This implies that the FIV mechanism in this region is unlikely to be galloping, since both ϕ_t and ϕ_v are out of phase with the body velocity by 90° (see Zhao et al., 2018a).

To understand better the flow structure associated with the FIV response regions, the near-body vorticity fields and swirling strength contours in the *x*–*y* plane are analysed based on spot PIV measurements. Following the eigen-decomposition of the three-dimensional local velocity gradient tensor (VGT) used by Zhou et al. (1996, 1999), an equivalent two-dimensional form is given by Adrian et al. (2000) for computing the VGT of PIV data in the *x*-*y* plane:

$$\nabla u = \begin{pmatrix} \dfrac{\partial u}{\partial x} & \dfrac{\partial v}{\partial x} \\ \dfrac{\partial u}{\partial y} & \dfrac{\partial v}{\partial y} \end{pmatrix}, \tag{2}$$

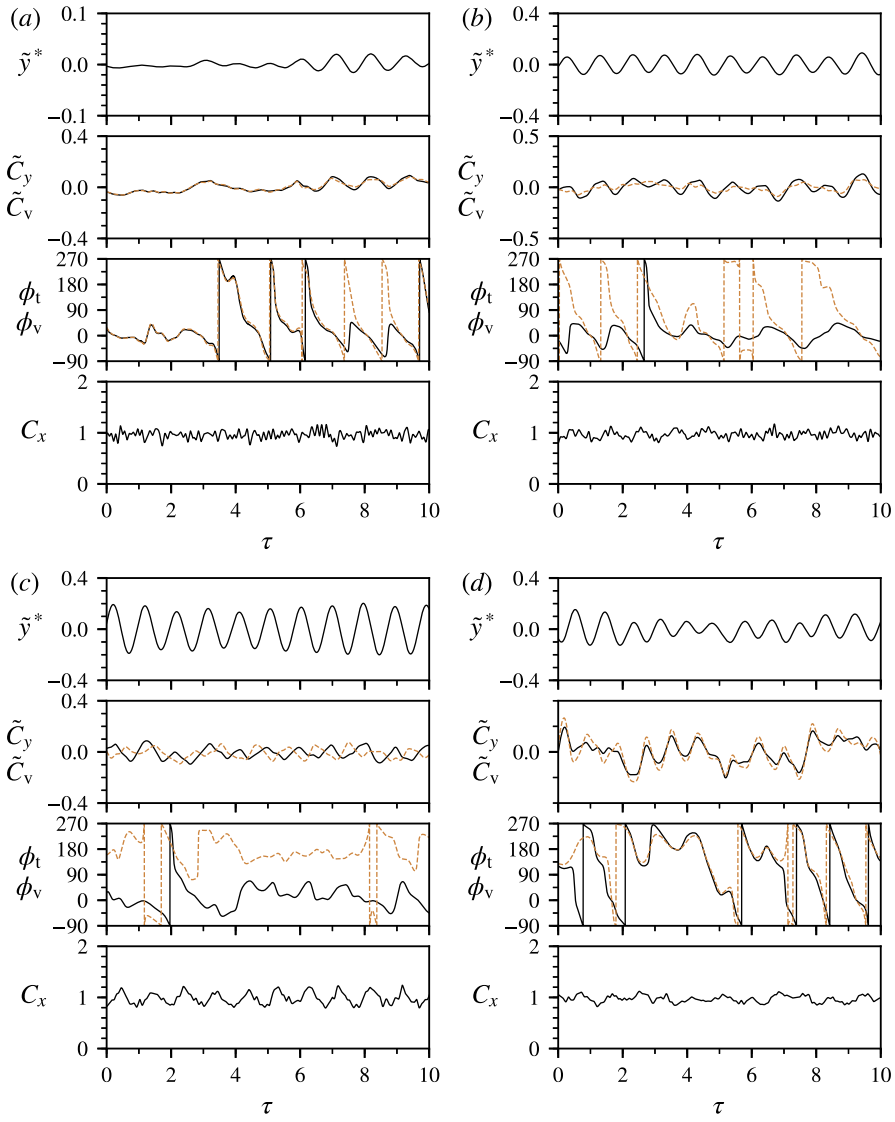

Fig. 12. Sample time traces the $\alpha = 20°$ case at four selected reduced velocities: $U^* = 5.0$ in (*a*), $U^* = 7.0$ in (*b*), $U^* = 9.0$ in (*c*) and $U^* = 12.0$ in (*d*).

where u and v are the (normalised) streamwise and cross-flow velocities, respectively. The resulting eigenvalues are either two real values (λ_r) or a pair of complex conjugate values ($\lambda_{cr} \pm i\lambda_{ci}$, with λ_{cr} and λ_{ci} the complex real and imaginary parts, respectively) as follows:

$$\begin{pmatrix} \lambda_r & 0 \\ 0 & \lambda_r \end{pmatrix} \tag{3}$$

or

$$\begin{pmatrix} \lambda_{cr} \pm i\lambda_{ci} & 0 \\ 0 & \lambda_{cr} \pm i\lambda_{ci} \end{pmatrix}. \tag{4}$$

Thus, the swirling strength is given by λ_{ci}^2, the square of the imaginary part of the complex conjugate eigenvalues (Zhou et al., 1999), and its sign is set to match that of the local vorticity to indicate the rotation direction. Compared to vorticity, swirling strength would be more useful to identify vortical structures (e.g. small-scale vortices), by eliminating pseudo-vorticity with no local spiralling motion, such as shear layers (see Zhou et al., 1999; Adrian et al., 2000; Chen et al., 2014).

Fig. 6 shows the phase-averaged vorticity and swirling strength contours at three reduced velocities ($U^* = 1.4$, 4.0 and 5.0) selected from the non-vibration regions. In these cases, the flow clearly separates from the forward corners, forming

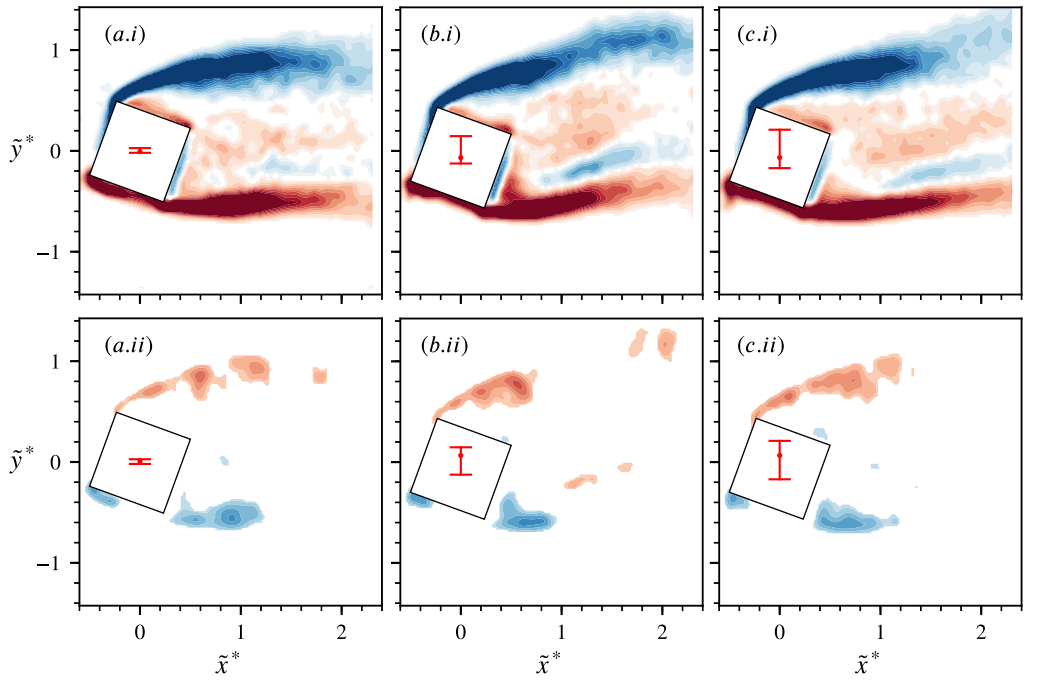

Fig. 13. Phase-averaged vorticity (top row) and swirling strength (bottom row) contours at (*a*) $U^* = 5.0$, (*b*) $U^* = 7.0$ and (*c*) $U^* = 12.0$ of the $\alpha = 20°$ case. See supplementary movies 10–12 for the full oscillation cycles. For more details, refer to the caption for Fig. 6.

two opposite-signed shear layers; however, there is neither flow reattachment observed, nor regular vortex shedding as in the case of a square cylinder (see Zhao et al., 2014b). Fig. 7 shows the phase-averaged vorticity contours of three representative cases for the Sync-I, transition and Sync-II regions, at $U^* = 3.0$, 7.0 and 10.0, respectively. (Note that animations of full oscillation cycles are provided in supplementary movies 4–6). In the case of $U^* = 3.0$ shown in Fig. 7(*a*), it can be seen that the body oscillation is associated with periodic shear layer impinging on the lateral sides of the cube. These shear layers appear to be much shorter than those seen in the non-vibration regions. Furthermore, the impinging shear layers interact with the backward corners of the body and break down further downstream. This is similar to the findings from wind-tunnel experiments by Nakamura et al. (1991) who reported that weak excitation associated with impinging-shear-layer instability occurred on a square cylinder at low reduced velocities centred around $U^* = 2.5$. Such an excitation is different from those of VIV and galloping, which are initiated by regular vortex shedding, at higher reduced velocities (e.g. Nemes et al., 2012; Zhao et al., 2014b). In the case of $U^* = 7.0$ from the transition region, the shear layers formed from the forward corners appear to be oscillatory, and they tend to impinge on the lateral sides as the body vibration increases with U^*. When U^* is further increased to the Sync-II region, as shown in Fig. 7(*c*), the shear layers exhibit periodic flapping behaviour on the body lateral sides and appear to have a stronger interaction with the trailing corners than the case in the transition region. As a result, the flow structures downstream of the trailing corners appear to be significantly different from those seen in the Sync-I region, leading to a different synchronisation (e.g. the $f^*_{C_X}$ response).

To better identify the near-body vortical structures, Fig. 8 shows the swirling strength contours of the aforementioned U^* cases. As can be seen, the swirling strength analysis also reveals that the Sync-I and Sync-II regions are associated with flow impingement.

Further evidence of impinging behaviour of the shear layers is presented in Fig. 9, which shows hydrogen-bubble flow visualisations at three different representative reduced velocities: $U^* = 3.0$ for Sync-I and $U^* = 10.0$ for Sync-II as compared against $U^* = 4.0$ for the non-vibration region. Note that the corresponding video records can be found in supplementary movies 7–9. Clearly, it can be seen in the snapshots in Fig. 9(*a*, *c*) that the body vibration is associated with shear layer impingement on the lateral sides of the cube in regions Sync-I and Sync-II, while in the case of negligible body vibration in Fig. 9(*b*) the shear layers are evidently separated from the body. These results are in accordance with the PIV measurements.

By contrast, the transverse FIV response of a cube at $\alpha = 0°$ is distinctly different from those of a square cylinder and a sphere. Bearman (1984) noted that vortex shedding behind a constant cross-section bluff body is reduced as the aspect ratio is reduced, and thus the forces generated by vortex shedding may become too weak to cause any significant oscillations for low-aspect-ratio bluff bodies; for example, Wootton (1969) observed in wind-tunnel experiments that significant VIV response was unlikely to occur for a circular cylinder with an aspect ratio less than 8. When compared against its counterpart square cylinder, the oscillating cube exhibits a distinctly different manner of vortex shedding,

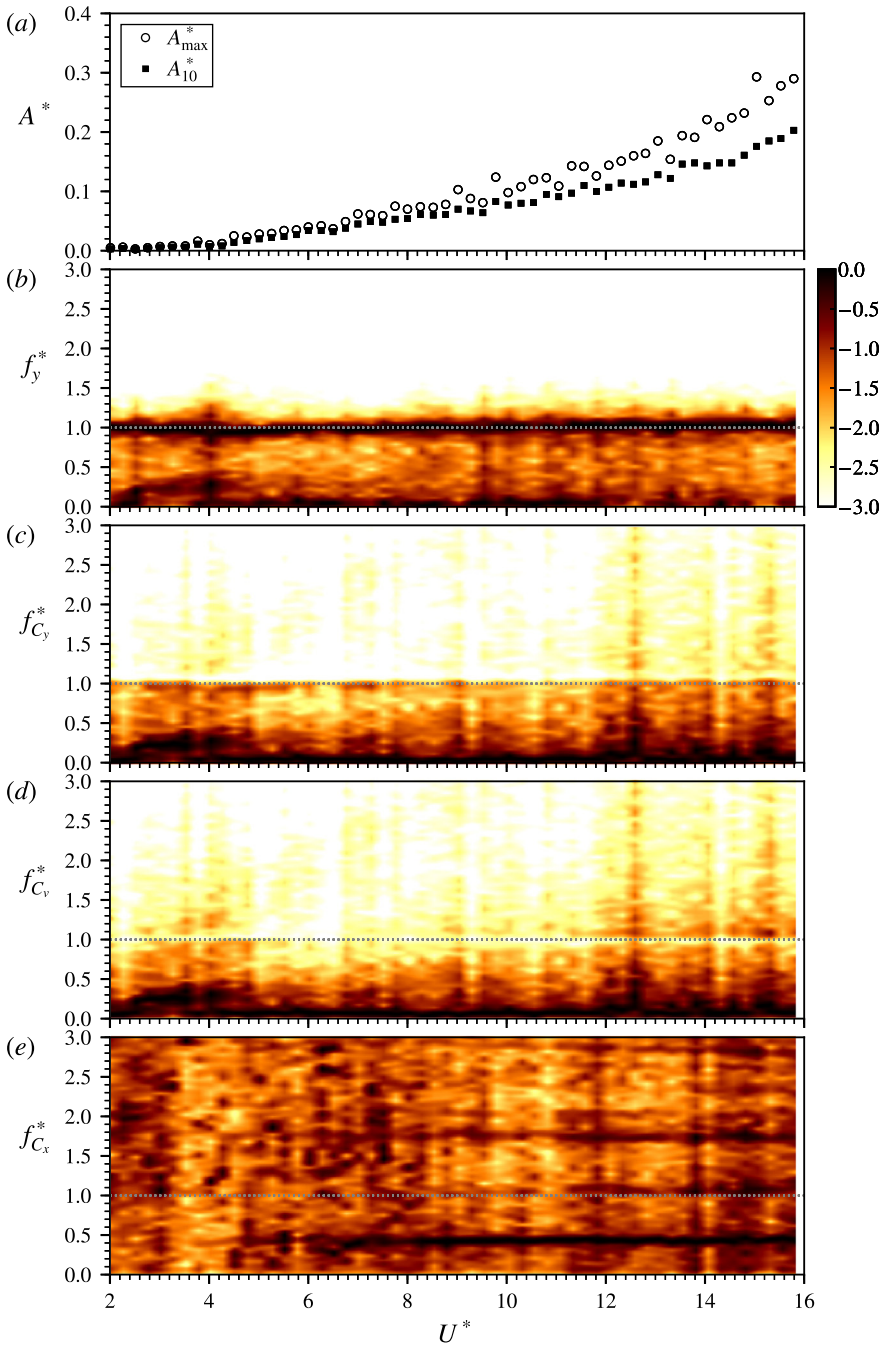

Fig. 14. The amplitude response and the logarithmic-scale normalised frequency power spectral density contours as a function of the reduced velocity for the case of $\alpha = 45°$.

where the two oppositely-signed shear layers appear to be well separated in the wake (e.g. Fig. 7(*c*)), while the square cylinder displays a regular vortex shedding mode with the shear layers strongly interacting to form a vortex street (see their figure 8 in Zhao et al. (2014b)). This difference is unsurprisingly expected as the vortex shedding of an fully immersed cube is three-dimensional, with the lateral shear layers affected by those formed from the top and bottom sides, thus resulting in a FIV response distinctly different from that of its counterpart square cylinder. Furthermore, the FIV response of a cube is also significantly different from that of a sphere. For example, the VIV of a sphere exhibits a typical amplitude jump when the body vibration frequency is close to the vortex shedding frequency of the static body at $U^* \approx 1/St \approx 5$. However, the cube exhibits an isolated lock-in region (Sync-I) at much lower reduced velocities, despite the fact that a

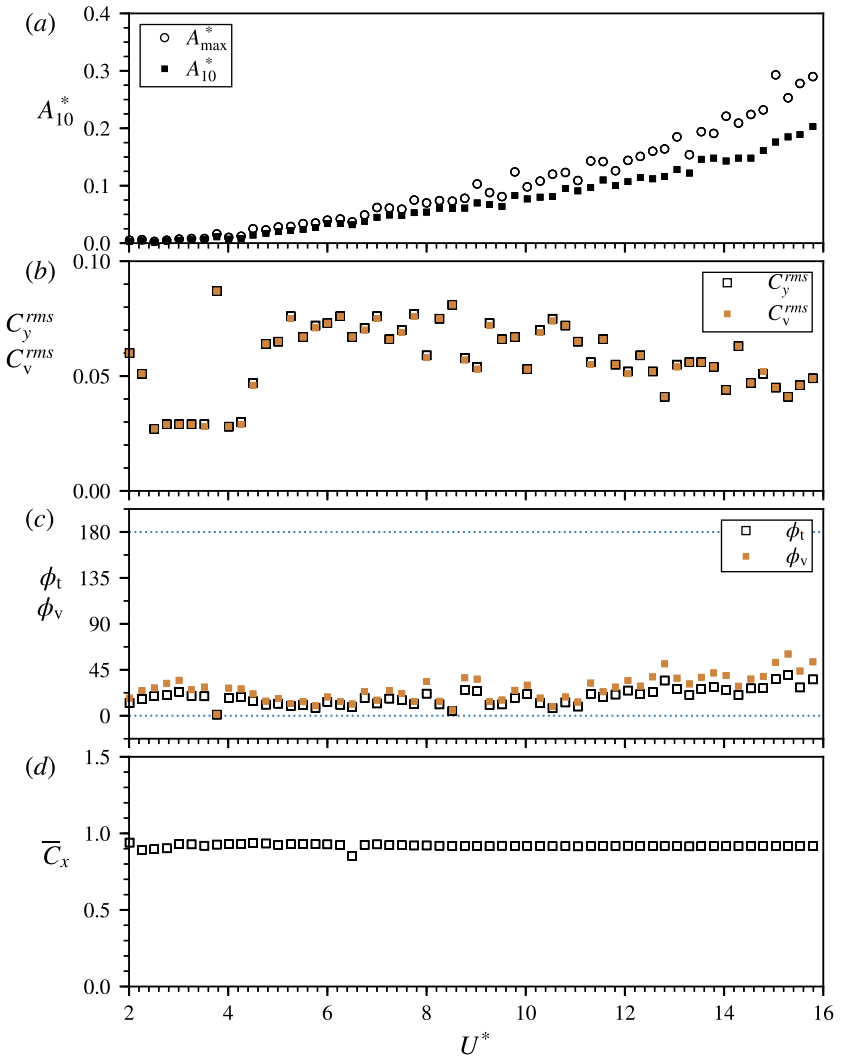

Fig. 15. Fluid forces and phases as a function of the reduced velocity for the $\alpha = 45°$ case.

second lock-in region occurs for $U^* \geqslant 8.4$ when the body vibration frequency approaches the Strouhal vortex shedding frequency. From the wake measurement results, it is evident that the mechanism driving the body vibration of a cube is different from that of a sphere: the transverse vibration of a cube is strongly associated with the shear layers that separate from the leading edges and impinge on the lateral sides of the body, while the sphere vibration is due to a counter-rotating vortex pair in the wake.

3.2. Vibration response at $\alpha = 20°$

Fig. 10 shows the amplitude and frequency responses as a function of the reduced velocity for the asymmetric case of $\alpha = 20°$, while Fig. 11 shows the variations of the fluid force coefficients and the phases. Through an overall examination of the above dynamic responses, a synchronisation region is identified over the reduced velocity range of $6.0 < U^* < 8.6$. In this region, while the body vibration frequency is synchronised with the transverse lift frequency, the vibration amplitude tends to increase gradually with U^* (i.e. $A^*_{max} \simeq 0.25$ at $U^* = 8.6$). Meanwhile, the C_y^{rms} variation profile exhibits a bell shape with its peak value of $C_y^{rms} \approx 0.07$ occurring at $U^* = 7.8$. On the other hand, ϕ_t becomes more stable close to 0° in this region. However, the $f^*_{C_v}$ response indicates that the vortex force is not periodic (see sample time traces at $U^* = 7$ in Fig. 12(b)), implying that the body vibration is most likely to be associated with the oscillation of shear layers. At higher U^* values outside the synchronisation region, considerable body oscillations (see Fig. 12(c, d)) are still caused by oscillatory shear layers; however, the frequency responses indicate that there is no synchronisation present. On the other hand, at low reduced velocities ($U^* < 6$) outside the synchronisation region, the body exhibits random vibration with extremely small amplitudes (see Fig. 12(a)).

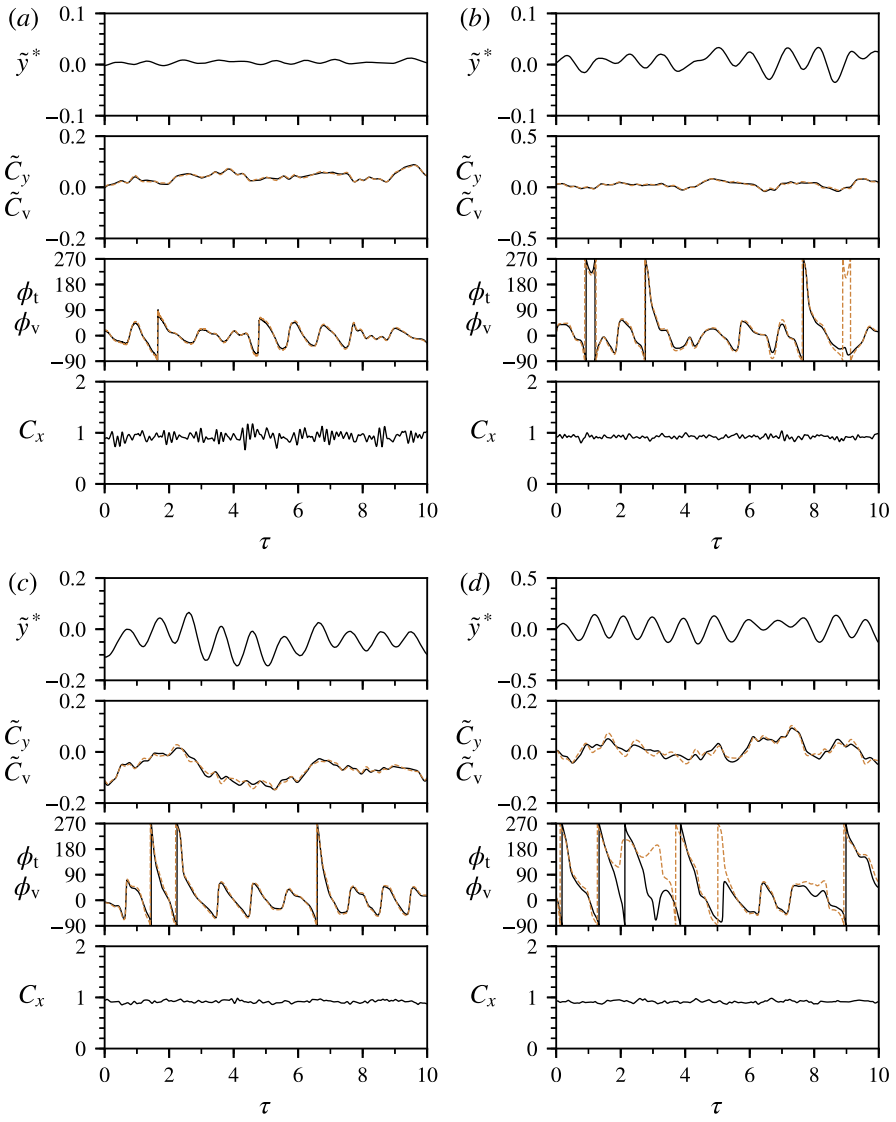

Fig. 16. Sample time traces of the $\alpha = 45°$ case at four selected reduced velocities: (*a*) $U^* = 5.0$, (*b*) $U^* = 6.0$, (*c*) $U^* = 12.0$ and (*d*) $U^* = 14.0$.

To demonstrate the near-field flow structure, Fig. 13 shows the phase-averaged vorticity and swirling strength contours at $U^* = 5.0$, 7.0, and 12.0, selected from different FIV response regions. In all cases, it is clear that the upper shear layer separates from the top corner, while lower shear layer wraps around the lower side and then separates from the lower trailing corner. The flow patterns in these cases appear to be highly similar. However, oscillatory behaviour of the shear layers can be seen in the supplementary movies; in particular, vortex structures can be seen being shed off the shear layers at $U^* = 7$ (in the synchronisation region) shown in supplementary movie 8. Again, unlike the cylinder case in Zhao et al. (2014b), which exhibits much larger vibration amplitudes that are associated with a 2S or 2(2S) vortex shedding mode, it is clear in the present case that the body vibration is due to the oscillatory shear layers.

3.3. Desynchronised vibration at $\alpha = 45°$

Fig. 14 shows the amplitude and frequency responses as a function of U^* for the $\alpha = 45°$ case. As evidenced by the frequency responses, the body vibration is desynchronised with the fluid forcing components over the U^* range tested. However, the vibration amplitude tends to increase with U^* ($A^*_{\text{max}} \approx 0.3$ at $U^* = 16$), while the forcing components C_y^{rms} and C_{v}^{rms} fluctuate around 0.06 over the entire U^* range (Fig. 15(*b*)). Moreover, similar to the case of 20°, the drag coefficient $\overline{C}_x$ remains consistently close to 0.9.

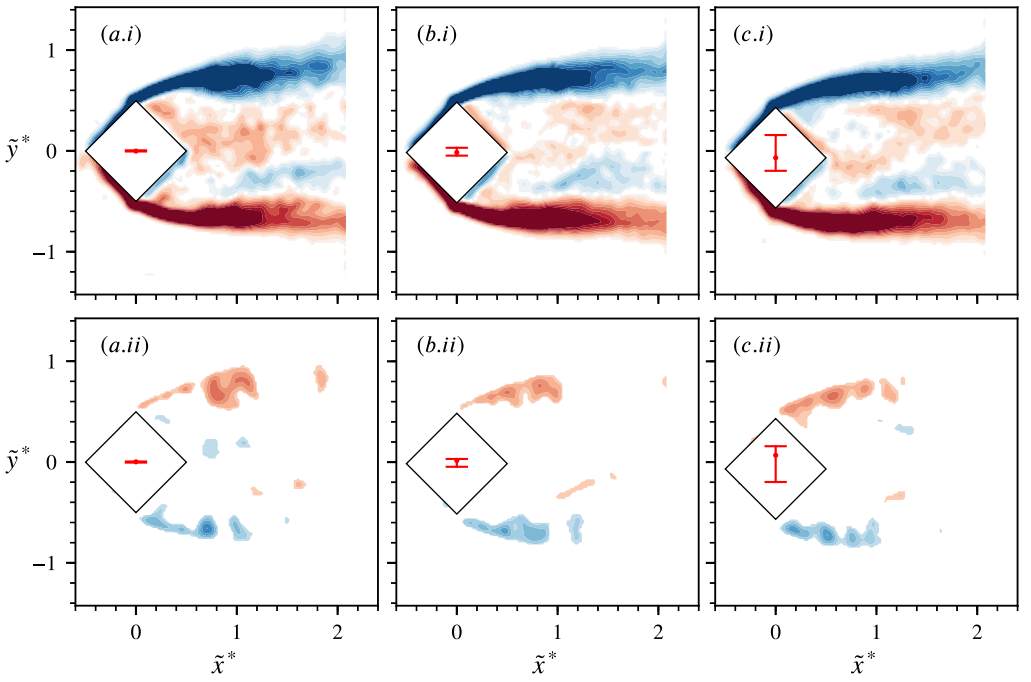

Fig. 17. Phase-averaged vorticity contours (top row) and swirling strength (bottom row) at (*a*) $U^* = 3.0$, (*b*) $U^* = 6.0$ and (*c*) $U^* = 14.0$ of the $\alpha = 45°$ case. See supplementary movies 13–15 for the full oscillation cycles. For more details, refer to the caption for Fig. 6.

Fig. 16 shows sample time traces of the dynamic components at four selected velocities, $U^* = 5$, 6, 12 and 14. In all cases, the dynamics appears to be highly aperiodic, consistent with the frequency responses in Fig. 14.

Fig. 17 shows the near-field vorticity and swirling strength contours from phase-averaged PIV measurements at $U^* = 3.0$, 6.0 and 14.0. As can be seen in all cases, two opposite-signed shear layers separate from the upper and lower sharp corners, and they appear to be oscillatory (see supplementary movies 10–12). However, the oscillatory shear layers are not synchronised with the body vibration.

Similar to the cases of $\alpha = 0°$ and 20°, the FIV response at $\alpha = 45°$ is also distinctly different from its cylinder counterpart that has been known to experience VIV response over a similar U^* range. Indeed, the results presented have indicated that the aspect ratio (of the body length to the side width) plays an important role affecting the flow and thus the dynamics.

4. Conclusions

This paper presents an experimental investigation on the transverse FIV of a cube at three angles of attack, $\alpha = 0°$, 20° and 45°, over a reduced velocity range of $1.2 \leqslant U^* \leqslant 16$.

At $\alpha = 0°$, it was found that the FIV response exhibits three vibration regions with significant oscillation amplitudes, namely the synchronisation Sync-I region (over $1.8 < U^* \leqslant 3.0$), the transition region (over $5.6 < U^* < 8.4$), and the synchronisation Sync-II region (for $U^* > 8.4$). In the Sync-I region, highly periodic body oscillations were encountered, with the oscillation frequency locked onto f_{nw}. The local amplitude peak was found to be $A^*_{max} \simeq 0.09$. The PIV measurements revealed that the body vibration is synchronised with periodic shear layer impinging behaviour, rather than regular well-defined vortex shedding as previously reported in the case of a square cylinder. After the Sync-I region, the system exhibited a "non-vibration" region, where the shear layers remained well separated from the forward corners, without reattachment onto the body. As U^* was increased, the shear layers tended to become oscillatory in the transition region, causing the body to vibrate. Further increasing U^* led to synchronisation between the body vibration and the shear-layer flapping in the Sync-II region. In this region, the vibration amplitude was observed to increase with U^*, i.e. $A^*_{max} \simeq 0.74$ at the highest U^* value tested.

For the asymmetric case of $\alpha = 20°$, a synchronisation region was observed to occur over $6.0 < U^* < 8.6$, where the body vibration frequency was synchronised with the transverse lift frequency. In this region, the vibration amplitude tended to increase with U^*, i.e. $A^*_{max} \simeq 0.25$ at $U^* = 8.6$. From the PIV measurements, it was found that the body vibration is due to oscillatory shear layers from which some vortex structures are shed off. However, at higher U^* values outside this region, although the oscillatory shear layers still caused the body to vibrate with considerable amplitude, the synchronisation disappeared.

For the $\alpha = 45^\circ$ case, similar to the other two α cases, the body vibration is caused by the oscillatory shear layers, but remains desynchronised through the entire U^* range tested. The vibration amplitude was found to increase with U^*, with the largest value of $A^*_{\text{max}} \approx 0.3$ observed at $U^* = 16$.

The findings presented have indicated that the body vibration is strongly coupled with the oscillatory shear layers which can result in significant vibration amplitudes. This study reveals that the FIV response of a cube is significantly different from its cylinder counterpart, the square cylinder. Interestingly, it is also distinctly different from that of a 1-DOF sphere even though the intermediate downstream wakes of non-oscillating spheres and cubes display similar wake structures. The closest match to the sphere FIV response was seen for the $\alpha = 20^\circ$ case, which shows a reduced VIV response over a similar reduced velocity range. In some sense, this appears to be related to the VIV response seen for a *rotating* sphere (Sareen et al., 2018a) where the rotation breaks the centreline mirror symmetry, causing a similar but reduced VIV response compared to a non-rotating sphere. The results here indicate the importance of the separating shear layers in the FIV response, while the absence of rotational symmetry seen for the circular cylinder or sphere cases allows a galloping response. Both these aspects alter the vibration response considerably.

Noting the importance of the separating shear layers, and the observed differences from the FIV response of cylinders and spheres, further work seems warranted to investigate the effect of the axial aspect ratio of a variable-span length square cross-section body.

Acknowledgement

The authors gratefully acknowledge the financial support from the Australian Research Council Discovery Project grants DP150102879 and DP170100275.

Appendix A. Supplementary data

Supplementary material related to this article can be found online at https://doi.org/10.1016/j.jfluidstructs.2019.102701.

References

Adrian, R.J., Christensen, K.T., Liu, Z.-C., 2000. Analysis and interpretation of instantaneous turbulent velocity fields. Exp. Fluids 29 (3), 275–290.
Bearman, P.W., 1984. Vortex shedding from oscillating bluff bodies. Annu. Rev. Fluid Mech. 16 (1), 195–222.
Bearman, P.W., Gartshore, I.S., Maull, D., Parkinson, G.V., 1987. Experiments on flow-induced vibration of a square-section cylinder. J. Fluids Struct. 1 (1), 19–34.
Blevins, R.D., 1990. Flow-Induced Vibration, second ed. Krieger Publishing Company, Malabar.
Brooks, P.N.H., 1960. Experimental Investigation of the Aeroelastic Instability of Bluff Two-Dimensional Cylinders (Masters). University of British Columbia.
Chen, W.-L., Li, H., Hu, H., 2014. An experimental study on the unsteady vortices and turbulent flow structures around twin-box-girder bridge deck models with different gap ratios. J. Wind Eng. Ind. Aerodyn. 132, 27–36.
Feng, C.C., 1968. The Measurement of Vortex Induced Effects in Flow Past Stationary and Oscillating Circular and D-Section Cylinders (M.A.Sc. Thesis). University of British Columbia.
Fouras, A., Lo Jacono, D., Hourigan, K., 2008. Target-free stereo PIV: a novel technique with inherent error estimation and improved accuracy. Exp. Fluids 44 (2), 317–329.
Govardhan, R., Williamson, C.H.K., 2000. Modes of vortex formation and frequency response of a freely vibrating cylinder. J. Fluid Mech. 420, 85–130.
Govardhan, R., Williamson, C.H.K., 2005. Vortex-induced vibrations of a sphere. J. Fluid Mech. 531, 11–47.
Khalak, A., Williamson, C.H.K., 1996. Dynamics of a hydroelastic cylinder with very low mass and damping. J. Fluids Struct. 10 (5), 455–472.
Khalak, A., Williamson, C.H.K., 1997. Fluid forces and dynamics of a hydroelastic structure with very low mass and damping. J. Fluids Struct. 11 (8), 973–982.
Klotz, L., Goujon-Durand, S., Rokicki, J., Wesfreid, J.E., 2014. Experimental investigation of flow behind a cube for moderate Reynolds numbers. J. Fluid Mech. 750, 73–98.
Lighthill, J., 1986. Fundamentals concerning wave loading on offshore structures. J. Fluid Mech. 173, 667–681.
Massai, T., Zhao, J., Lo Jacono, D., Bartoli, G., Sheridan, J., 2018. The effect of angle of attack on flow-induced vibration of low-side-ratio rectangular cylinders. J. Fluids Struct. 82, 375–393.
Mirauda, D., Volpe Plantamura, A., Malavasi, S., 2014. Dynamic response of a sphere immersed in a shallow water flow. J. Offshore Mech. Arct. Eng. 136 (2), 021101.
Morse, T.L., Williamson, C.H.K., 2009. Prediction of vortex-induced vibration response by employing controlled motion. J. Fluid Mech. 634, 5–39.
Nakamura, Y., Hirata, K., Urabe, T., 1991. Galloping of rectangular cylinders in the presence of a splitter plate. J. Fluids Struct. 5 (5), 521–549.
Naudascher, E., Rockwell, D., 2005. Flow-Induced Vibrations: An Engineering Guide. Dover Publications.
Nemes, A., Zhao, J., Lo Jacono, D., Sheridan, J., 2012. The interaction between flow-induced vibration mechanisms of a square cylinder with varying angles of attack. J. Fluid Mech. 710 (102).
Païdoussis, M., Price, S., de Langre, E., 2010. Fluid-Structure Interactions: Cross-Flow-Induced Instabilities. Cambridge University Press.
Saha, A.K., 2004. Three-dimensional numerical simulations of the transition of flow past a cube. Phys. Fluids 16, 1630–1646.
Saha, A., 2006. Three-dimensional numerical study of flow and heat transfer from a cube placed in a uniform flow. Int. J. Heat Fluid Flow 27 (1), 80–94.
Sareen, A., Zhao, J., Lo Jacono, D., Sheridan, J., Hourigan, K., Thompson, M.C., 2018a. Vortex-induced vibration of a rotating sphere. J. Fluid Mech. 837, 258–292.
Sareen, A., Zhao, J., Sheridan, J., Hourigan, K., Thompson, M., 2018b. Vortex-induced vibrations of a sphere close to a free surface. J. Fluid Mech. 846, 1023–1058.
Sarpkaya, T., 2004. A critical review of the intrinsic nature of vortex-induced vibrations. J. Fluids Struct. 19 (4), 389–447.

Soti, A.K., Zhao, J., Thompson, M.C., Sheridan, J., Bhardwaj, R., 2018. Damping effects on vortex-induced vibration of a circular cylinder and implications for power extraction. J. Fluids Struct. 81, 289–308.
Wang, Z., Du, L., Zhao, J., Sun, X., 2017. Structural response and energy extraction of a fully passive flapping foil. J. Fluids Struct. 72, 96–113.
Williamson, C.H.K., Govardhan, R., 2004. Vortex-induced vibration. Annu. Rev. Fluid Mech. 36, 413–455.
Wong, K.W.L., Zhao, J., Lo Jacono, D., Thompson, M.C., Sheridan, J., 2017. Experimental investigation of flow-induced vibration of a rotating circular cylinder. J. Fluid Mech. 829, 486–511.
Wong, K.W.L., Zhao, J., Lo Jacono, D., Thompson, M.C., Sheridan, J., 2018. Experimental investigation of flow-induced vibration of a sinusoidally rotating circular cylinder. J. Fluid Mech. 848, 430–466.
Wootton, L.R., 1969. The oscillation of large circular stacks in wind. Proc. Inst. Civ. Eng. 43, 573–598.
Zhao, J., Hourigan, K., Thompson, M.C., 2018a. Flow-induced vibration of D-section cylinders: an afterbody is not essential for vortex induced vibration. J. Fluid Mech. 851, 317–343.
Zhao, J., Leontini, J.S., Lo Jacono, D., Sheridan, J., 2014a. Chaotic vortex induced vibrations. Phys. Fluids 26 (12), 121702.
Zhao, J., Leontini, J.S., Lo Jacono, D., Sheridan, J., 2014b. Fluid–structure interaction of a square cylinder at different angles of attack. J. Fluid Mech. 747, 688–721.
Zhao, J., Lo Jacono, D., Sheridan, J., Hourigan, K., Thompson, M.C., 2018b. Experimental investigation of in-line flow-induced vibration of a rotating cylinder. J. Fluid Mech. 847, 664–699.
Zhao, J., Nemes, A., Lo Jacono, D., Sheridan, J., 2018c. Branch/mode competition in the flow-induced vibration of a square cylinder. Philos. Trans. R. Soc. Lond. Ser. A 376, 201702.
Zhou, J., Adrian, R.J., Balachandar, S., 1996. Autogeneration of near-wall vortical structures in channel flow. Phys. Fluids 8 (1), 288–290.
Zhou, J., Adrian, R.J., Balachandar, S., Kendall, T., 1999. Mechanisms for generating coherent packets of hairpin vortices in channel flow. J. Fluid Mech. 387, 353–396.